LIGHT SCATTERING BY PATHOLOGICAL AND DEFORMED ERYTHROCYTES: AN INTEGRAL EQUATION MODEL

Nikolaos K. Uzunoglu,[†] **Dido Yova,**[†] **and Georgios S. Stamatakos**[‡]

[†]National Technical University of Athens, Division of Electroscience, Department of Electrical and Computer Engineering, Zografou Campus, GR-157 80 Athens, Greece; [‡]National Technical University of Athens, Department of Physics, Zografou Campus, GR-157 80 Athens, Greece

ABSTRACT

A novel mathematical model of light scattering by pathological and deformed erythrocytes is presented. An erythrocyte is modeled as a homogeneous triaxial dielectric ellipsoid of complex index of refraction. Both its position and orientation in a given cartesian coordinate system are considered arbitrary. The analysis is based on the Lippman–Schwinger integral equation for the electric field. The corresponding (singular) integral equation for the scattering is transformed into an integral equation for the Fourier transform of the electric field inside the scatterer. The latter equation has a nonsingular kernel. It is solved by reducing it by quadrature into a linear set of equations. The resulting solutions are used to calculate the scattering amplitude. Several tests ensuring the validity of the approach along with sample calculations are presented. © *1997 Society of Photo-Optical Instrumentation Engineers.* [S1083-3668(97)00703-X]

Keywords light scattering, erythrocytes, erythrocyte deformability, ectacytometry, flow cytometry.

1 INTRODUCTION

Light scattering by cells has proved to be a powerful diagnostic tool in various biomedical applications. In laser flow cytometry, it provides information on the size, the shape, and the biochemical composition of cells.[1] In ectacytometry, it is used to determine both the deformability[2] and the stress-induced rigidification of erythrocytes,[3] whereas in syllectometry, it is employed to quantify their tendency for aggregation.[4] It has been established that both the deformability and the tendency for aggregation of eryrthrocytes play an important role in micro- and macrocirculation.[5]

This paper focuses on the study of the morphological and mechanical characteristics of red blood cells (RBCs) by optical methods. We noticed that certain shapes of pathological[6] and deformed RBCs may be considered special cases of a general triaxial ellipsoid. For example, both an artificially sphered RBC (as it is sometimes used in flow cytometry) and a spherocyte have a nearly spherical shape (three equal semiaxes). An oblate spheroid may model an RBC when it constitutes part of an RBC rouleau.[7] A triaxial prolate ellipsoid is the exact shape of a mechanically deformed RBC when it is subjected to high shear stress (e.g., in ectacytometry).[8] It is also practically the shape of a pathological elliptocyte. Furthermore, other shapes

of erythrocytes might be approached, although less satisfactorily, by the shape of a general triaxial ellipsoid. Examples include the approximation of a normal RBC at rest by an oblate spheroid (the exact shape of an RBC at rest is a biconcave disk, however), the approximation of a drepanocyte by a prolate triaxial ellipsoid (drepanocytes are rather sickle shaped), and the approximation of a leptocyte by an oblate spheroid (leptocytes are thin, flat, biconcave cells).[6]

Various existing theoretical treatments are applicable to certain special cases of interest. As indicative examples, we mention the Mie theory applicable to spherical RBCs,[9] the modal series expansion of electromagnetic field in terms of prolate spheroidal vector functions applicable to prolate spheroidal RBCs,[10] and the approximate van de Hulst anomalous diffraction theory[11] applicable to triaxial ellipsoidal RBCs.[8] Nevertheless, there is no efficient, non-*a priori* approximate treatment for the scattering of light by triaxial ellipsoidal erythrocytes.

In this paper a non-*a priori* approximate mathematical analysis of light scattering by a triaxial dielectric ellipsoid of complex index of refraction is developed. The analysis is based on the theory of Fredholm integral equations and is referred to as the Fredholm integral equation model or FIEM. The integral equation approach to solving complex electromagnetic boundary value problems has been

---

Address all correspondence to Nikolaos Uzunoglu. Tel: 301 772 3556; Fax: 301 772 3557; E-mail: nuzu@central.ntua.gr.

well established and verified. Both the position and the orientation of the scatterer in a given cartesian coordinate system are considered arbitrary. The case of a large scatterer can obviously be dealt with. FIEM is applied to the case of pathological and deformed erythrocytes with the intention of gaining insight into the light scattering phenomena encountered in various optical diagnostic techniques in hematology. Thus, a novel theoretical tool is provided for the recently emerged areas of flow cytometry and hemorheology that is useful for the optical determination of the geometrical and the mechanical characteristics of erythrocytes.

The present work has its origins in Refs. 12 and 13, where scattering of electromagnetic radiation by resonance-size ellipsoids placed at the origin of a cartesian coordinate system was considered. The numerical applications performed in those works, however, concerned scatterers with small size parameters (e.g., $k_0 a = 0.4$). In the present paper, size parameters are rather high (e.g., $k_0 a = 37$). This leads to high computing time demands. Consequently, new computational problems have to be tackled.

The main steps of the analysis are as follows. (1) The Lippman–Schwingwer integral equation for the electric field is formulated. (2) The scattering amplitude equation is deduced by using the limit of the previous equation, while the distance between the point of observation and the center of the scatterer system tends to infinity. (3) The (singular) Lippman–Schwinger equation for the electric field is transformed into an integral equation for the angular Fourier transform of the electric field inside the scatterer. The transformed equation has a nonsingular kernel. (4) The latter equation is reduced by quadrature into a matrix equation. (5) The resulting solutions are used to calculate the scattering amplitude.

2 THEORY

2.1 THE MODEL

An RBC is modeled (in the general case) as a tri-axial homogeneous dielectric ellipsoid with semi-axes a_1, b_1, c_1. For $a_1 = b_1$ and $c_1 < a_1$, the shape of an oblate spheroid is obtained, whereas for $a_1 = b_1$ and $c_1 > a_1$ the shape of a prolate spheroid is produced. The index of refraction n_0 relative to the suspending medium and consequently the relative dielectric constant $\epsilon = n_0^2$ of the RBC for a given wavelength are considered complex. The index of refraction of the suspending medium (which may be either plasma or any other optically equivalent and isotonic liquid) is considered real, given that plasma has a very low optical absorption in the visible range of the spectrum. Most diagnostic instruments operate in this range.

Dyadic notation is used throughout the analysis. The following two cartesian systems are used: the
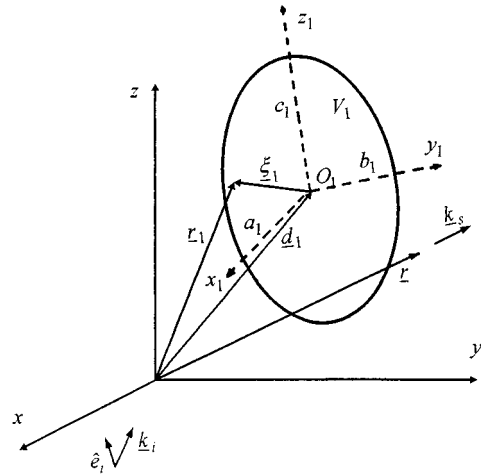

Fig. 1 The cartesian coordinate systems used in the analysis.

"absolute" system, xyz and the local one, $x_1 y_1 z_1$ with its origin at the center of the ellipsoid V_1 (Figure 1). The ellipsoid V_1 is defined in the local coordinate system $x_1 y_1 z_1$ by the equation

$$\frac{x_1^2}{a_1^2} + \frac{y_1^2}{b_1^2} + \frac{z_1^2}{c_1^2} = 1. \tag{1}$$

The following symbol conventions are used throughout the analysis. X denotes a scalar quantity (generally a complex number). $\underline{X}$, $\underline{\underline{X}}$ denote vectors (generally of complex elements). $\hat{X}$, $\underline{\hat{X}}$, $\underline{\hat{\underline{X}}}$ denote unit vectors (of real elements). $\bar{X}$ denotes a matrix or a dyadic (generally of complex elements). A product sign at the beginning of an equation continuation line stands for a scalar product.

A plane electromagnetic wave of wave vector $\underline{k}_i = k_0 \hat{k}_i$ and polarization $\hat{e}_i$ is incident on the ellipsoid. The time dependence is taken as $\exp(-i\omega t)$ and is suppressed throughout the analysis. The electric field (dyadic) at any point $\underline{r}$ in the xyz coordinate system is given by Ref. 14

$$\bar{E}(\underline{r}) = \bar{J}_i \exp(i\underline{k}_i \underline{r}) + \int_{V_1} d\underline{r}_1 \gamma \bar{G}(\underline{r}, \underline{r}_1) \cdot \bar{E}(\underline{r}_1), \tag{2}$$

where

$$\gamma = \frac{k_0^2}{4\pi}(\epsilon - 1), \tag{3}$$

k_0 is the suspending medium propagation constant, $\bar{1}$ is the unit dyadic, and for any subscript λ

$$\bar{J}_\lambda = \bar{1} - \hat{k}_\lambda \hat{k}_\lambda, \tag{4}$$

$\hat{k}_\lambda$ is a unit vector along $\underline{k}_\lambda$,

$$\bar{G}(\underline{r}, \underline{r}_1) = (\bar{1} + k_0^{-2} \nabla \nabla) G(\underline{r}, \underline{r}_1) \tag{5}$$

and

$$G(\underline{r},\underline{r}_1)=\frac{\exp(ik_0|\underline{r}-\underline{r}_1|)}{|\underline{r}-\underline{r}_1|}. \qquad (6)$$

In order to obtain the plane plus scattered wave for an incident wave $\hat{e}_i E_0 \exp(i\underline{k}_i\cdot\underline{r})$, both sides of (2) should be multiplied by $\hat{e}_i E_0$. If the vector ξ_1 is expressed in the local coordinate system $x_1 y_1 z_1$, the following relations hold

$$\underline{r}_1=\underline{d}_1+\bar{A}_1\cdot\xi_1 \qquad (7)$$

where $\bar{A}_1$ is an appropriate rotation matrix given below and

$$d\underline{r}_1=d\xi_1. \qquad (8)$$

The xyz coordinate system may be considered as originating from the $x_1 y_1 z_1$ local coordinate system by rotation and translation as follows. The $x_1 y_1 z_1$ system is rotated about its original z_1 axis by the ψ_1 angle $(0\leqslant\psi_1\leqslant 2\pi)$; the transformed system is rotated about its new y_1 axis by the θ_1 angle $(-\pi/2\leqslant\vartheta_1\leqslant\pi/2)$; and the latter system is rotated about its new x_1 axis by the ω_1 angle $(0\leqslant\omega_1\leqslant 2\pi)$. The emerged system is translated by the vector $-\underline{d}_1$ so that the xyz coordinate system is obtained. Then the $\bar{A}_1$ matrix is given by Ref. 15

$$\bar{A}_1=\begin{bmatrix} \cos(\psi_1)\cos(\theta_1) & \sin(\psi_1)\cos(\vartheta_1) & -\sin(\vartheta_1) \\ [-\sin(\psi_1)\cos(\omega_1)+\cos(\psi_1)\sin(\theta_1)\sin(\omega_1)] & [\cos(\psi_1)\cos(\omega_1)+\sin(\psi_1)\sin(\vartheta_1)\sin(\omega_1)] & \cos(\vartheta_1)\sin(\omega_1) \\ [\sin(\psi_1)\sin(\omega_1)+\cos(\psi_1)\sin(\vartheta_1)\cos(\omega_1)] & [-\cos(\psi_1)\sin(\omega_1)+\sin(\psi_1)\sin(\vartheta_1)\cos(\omega_1)] & \cos(\vartheta_1)\cos(\omega_1) \end{bmatrix}. \qquad (9)$$

The dyadic scattering amplitude $\bar{f}(\underline{k}_s,\underline{k}_i)$ for scattering in the direction of $\underline{k}_s=k_0\hat{k}_s$ is defined by

$$\bar{E}(\underline{r})\xrightarrow[r\to\infty]{}\bar{I}_i\exp(i\underline{k}_i\cdot\underline{r})+\frac{\exp(ik_0 r)}{r}\bar{f}(\underline{k}_s,\underline{k}_i)$$

$$+0\left(\frac{1}{r^2}\right), \qquad (10)$$

where $r=|\underline{r}|$.

Considering the asymptotic form of (2) as $r\to\infty$ gives

$$\lim_{r\to\infty}\bar{E}(\underline{r})=\bar{I}_i\exp(i\underline{k}_i\cdot\underline{r})+\frac{\exp(ik_0 r)}{r}\bar{I}_s\int_{V_1}\gamma$$

$$\times\exp(-i\underline{k}_s\cdot\underline{r}_1)\bar{E}(\underline{r}_1)d\underline{r}_1. \qquad (11)$$

Therefore the dyadic scattering amplitude is expressed as

$$\bar{f}(\underline{k}_s,\underline{k}_i)=\bar{I}_s\cdot\int_{V_1}\gamma\exp(-i\underline{k}_s\cdot\underline{r}_1)\bar{E}(\underline{r}_1)d\underline{r}_1 \qquad (12)$$

and the vector scattering amplitude for incident wave polarization $\hat{e}_i$ is given by

$$\underline{f}(\underline{k}_s,\underline{k}_i,\hat{e}_i)=\bar{f}(\underline{k}_s,\underline{k}_i)\cdot\hat{e}_i. \qquad (13)$$

2.2 METHOD OF SOLUTION

The field equation (2) is an integral equation with a singular kernel. In what follows, a method is applied that deals with the singularity analytically,

leaving an integral equation with nonsingular kernel.[16] Multiplying (2) by $(\gamma/k_0^2)\exp(-i\underline{k}_1\cdot\underline{r})$, where $\underline{k}_1=k_1\hat{k}_1$ is at present an arbitrary vector (expressed in the xyz system,) and integrating throughout the volume of the scatterer V_1 gives

$$\frac{1}{k_0^2}\int_{V_1}\gamma\exp(-i\underline{k}_1\cdot\underline{r})\bar{E}(\underline{r})d\underline{r}$$

$$=\bar{I}_i\frac{1}{k_0^2}\int_{V_1}\gamma\exp[(\underline{k}_i-\underline{k}_1)\cdot\underline{r}]d\underline{r}$$

$$+\frac{1}{k_0^2}\int_{V_1}d\underline{r}\,\gamma\exp(-i\underline{k}_1\cdot\underline{r})\int_{V_1}d\underline{r}_1\gamma$$

$$\times\bar{G}(\underline{r},\underline{r}_1)\cdot\bar{E}(\underline{r}_1). \qquad (14)$$

The electric field inside the scatterer V_1 is expressed as the angular Fourier transform (in the xyz coordinate system)

$$\bar{E}(\underline{r}_1)=\int d\underline{k}_2\bar{C}_1(\underline{k}_2)\exp(i\underline{k}_2\cdot\underline{r}_1), \qquad (15)$$

where

$$\underline{k}_2=k_2\hat{k}_2. \qquad (16)$$

Substituting (15) into (14) gives

$$\int d\underline{k}_2\bar{K}(\underline{k}_1,\underline{k}_2)\cdot\bar{C}_1(\underline{k}_2)=\bar{I}_i U_{V_1}(\underline{k}_1,\underline{k}_i) \quad \text{for any } \underline{k}_1, \qquad (17)$$

where

$$U_{V_1}(\underline{k}_1,\underline{k}_2)=\frac{1}{k_0^2}\int_{V_1}\gamma\,\exp[-i(\underline{k}_1-\underline{k}_2)\cdot\underline{r}_1]d\underline{r}_1$$

$$\text{for any } \underline{k}_1,\underline{k}_2 \qquad (18)$$

and

$$\bar{K}(\underline{k}_1,\underline{k}_2)=\bar{\underline{1}}U_{V_1}(\underline{k}_1,\underline{k}_2)-\frac{1}{k_0^2}\int_{V_1}d\underline{r}'_1\int_{V_1}d\underline{r}_1\gamma$$

$$\times\exp(-i\underline{k}_1\cdot\underline{r}'_1)\bar{\underline{G}}(\underline{r}'_1,\underline{r}_1)\gamma\,\exp(i\underline{k}_2\cdot\underline{r}_1).$$

$$(19)$$

Performing mathematical manipulations similar to those presented in Ref. 17 for the calculation of the matrix element $\bar{K}^{aa}(\underline{k}_1,\underline{k}_2)$, the following expression for $\bar{K}(\underline{k}_1,\underline{k}_2)$ is obtained.

$$\bar{K}(\underline{k}_1,\underline{k}_2)=\exp[-i(\underline{k}_1-\underline{k}_2)\cdot\underline{d}_1]\left[\bar{\underline{1}}\epsilon(\epsilon-1)\right.$$

$$\times a_1b_1c_1\frac{j_1(|\underline{K}_{11}-\underline{K}_{21}|_c)}{|\underline{K}_{11}-\underline{K}_{21}|_c}-\frac{(\epsilon-1)^2}{2\pi^2}$$

$$\times(a_1b_1c_1)^2\pi ik_0\int_0^1 dx_p\int_0^{2\pi}d\varphi_p(\bar{\underline{1}}-\hat{p}\hat{p})$$

$$\times\sum_{\substack{n=0\\n+m=}}^{\infty}\sum_{\substack{m=0\\\text{even}}}^{\infty}(2n+3)(2m+3)$$

$$\times\frac{j_{n+1}(|\underline{K}_{11}|_c)}{|\underline{K}_{11}|_c}\frac{j_{m+1}(|\underline{K}_{21}|_c)}{|\underline{K}_{21}|_c}$$

$$\times\frac{j_{m_>+1}(k_0Y)h_{m_<+1}(k_0Y)}{Y^2}$$

$$\left.\times T_n^1(\hat{\underline{P}}_1\cdot\hat{\underline{K}}_{11})T_m^1(\hat{\underline{P}}_1\cdot\hat{\underline{K}}_{21})\right], \qquad (20)$$

where the following symbols have been used (including those of some intermediate steps): $j_n(z)$ is the complex spherical Bessel function of order n.

The symbol $|\ |_c$ is defined by the relation

$$|\underline{A}-\underline{B}|_c=\sqrt{A^2+B^2-2\underline{A}\cdot\underline{B}}, \qquad (21)$$

where

$$\underline{A}=A\hat{A}, \qquad (22)$$

$$\underline{B}=B\hat{B}. \qquad (23)$$

(A, B are generally complex numbers.) The symbol $\sqrt{z}=[r\,\exp(i\varphi)]^{1/2}$ denotes the complex square root $r^{1/2}\exp(i(\varphi/2))$,

$$m_>=\max\{m,n\},\quad m_<=\min\{m,n\} \qquad (24)$$

$$h_n(z)=\left(\frac{\pi}{2z}\right)^{1/2}H_{n+1/2}^{(1)}(z)$$

$$\text{(spherical Hankel function)}, \qquad (25)$$

$$x_a=\cos(\vartheta_a)\quad\text{for any subscript }a, \qquad (26)$$

$$\underline{P}_1=p(\sqrt{1-x_p^2}\,\cos\,\varphi_p,\sqrt{1-x_p^2}\,\sin\,\varphi_p,x_p)\cdot\bar{\underline{A}}_1$$

$$\equiv p(Z_x,Z_y,Z_z), \qquad (27)$$

$$\hat{\underline{P}}_1=\frac{1}{Y}\,(a_1Z_x,b_1Z_y,c_1Z_z), \qquad (28)$$

$$Y=[a_1^2Z_x^2+b_1^2Z_y^2+c_1^2Z_z^2]^{1/2}, \qquad (29)$$

$$\underline{K}_{11}=k_1(\sqrt{1-x_{k_1}^2}\,\cos\,\phi_{k_1},\sqrt{1-x_{k_1}^2}\,\sin\,\varphi_{k_1},x_{k_1})\cdot\bar{\underline{A}}_1$$

$$\equiv k_1(H_x,H_y,H_z), \qquad (30)$$

(k_1 can take complex values)

$$\underline{K}_{11}=k_1(a_1H_x,b_1H_y,c_1H_z), \qquad (31)$$

$$|\underline{K}_{11}|_c=n_0k_0(a_1^2H_x^2+b_1^2H_y^2+c_1^2H_z^2)^{1/2}, \qquad (32)$$

$$\hat{\underline{K}}_{11}=\frac{1}{(a_1^2H_x^2+b_1^2H_y^2+c_1^2H_z^2)^{1/2}}\,(a_1H_x,b_1H_y,c_1H_z),$$

$$(33)$$

$$\underline{K}_{21}=k_2(\sqrt{1-x_{k_2}^2}\,\cos\,\varphi_{k_2},\sqrt{1-x_{k_2}^2}\,\sin\,\varphi_{k_2},x_{k_2})\cdot\bar{\underline{A}}_1$$

$$\equiv k_2(\Lambda_x,\Lambda_y,\Lambda_z), \qquad (34)$$

$$\underline{K}_{21}=k_2(a_1\Lambda_x,b_1\Lambda_y,c_1\Lambda_z), \qquad (35)$$

(k_2 can take complex values). For homogeneous scatterers $k_1=k_2=k_0n_0$.

$$|\underline{K}_{21}|_c=n_0k_0\sqrt{a_1^2\Lambda_x^2+b_1^2\Lambda_y^2+c_1^2\Lambda_z^2} \qquad (36)$$

and

$$\hat{\underline{K}}_{21}=\frac{1}{(a_1^2\Lambda_x^2+b_1^2\Lambda_y^2+c_1^2\Lambda_z^2)^{1/2}}\,(a_1\Lambda_x,b_1\Lambda_y,c_1\Lambda_z).$$

$$(37)$$

$T_n^1(x)$ is the Gegenbauer function. Note that the $\underline{K}_{11},\underline{K}_{21}$, and $\underline{P}_1$ vectors are expressed in the local coordinate system $x_1y_1z_1$.

The dyadic $\bar{\underline{1}}-\hat{p}\hat{p}$ has the representation

$$\bar{1}-\hat{p}\hat{p}=\begin{bmatrix} 1-y^2\cos^2\varphi_p & -y^2\cos\varphi_p\sin\varphi_p & -xy\cos\varphi_p \\ -y^2\cos\varphi_p\sin\varphi_p & 1-y^2\sin^2\varphi_p & -xy\sin\varphi_p \\ -xy\cos\varphi_p & -xy\sin\varphi_p & y^2 \end{bmatrix},\qquad(38)$$

where $x=\cos\vartheta_p$ and $y^2=1-x^2$,

The right part of Eq. (17) becomes

$$\bar{J}_i U_{V_1}(\underline{k}_1,\underline{k}_i)=(\bar{1}-\hat{k}_i\hat{k}_i)\exp[-i(\underline{k}_1-\underline{k}_i)\cdot\underline{d}_1]a_1b_1c_1$$

$$\times(\epsilon-1)\frac{j_1(|\underline{\underline{K}}_{11}-\underline{\underline{K}}_{i1}|_c)}{|\underline{\underline{K}}_{11}-\underline{\underline{K}}_{i1}|_c},\qquad(39)$$

where

$$\underline{K}_{i1}=k_0(\sqrt{1-x_{k_i}^2}\cos\varphi_{k_i},\sqrt{1-x_{k_i}^2}\sin\varphi_{k_i},x_{k_i})\cdot\bar{A}_1$$

$$\equiv k_0(\Sigma_x,\Sigma_y,\Sigma_z)\qquad(40)$$

and

$$\underline{K}_{i1}=k_0(a_1\Sigma_x,b_1\Sigma_y,c_1\Sigma_z).\qquad(41)$$

Substituting (15) into (12) gives

$$\bar{f}(\underline{k}_s,\underline{k}_i)=k_0^2\bar{J}_s\cdot\int U_{V_1}(\underline{k}_s,\underline{k}_2)\bar{C}_1(\underline{k}_2)d\underline{k}_2.\qquad(42)$$

The integral Eq. (17) is reduced by quadrature into a set of linear equations (a matrix equation). If we choose the $\underline{k}_2$ pivots and weights to be the set

$$S=\{\underline{\kappa}_j,w_j|j=1,\dots n'\},\qquad(43)$$

the arbitrary $\underline{k}_1$ is restricted to a maximum of n' arbitrary values. We choose these to be those of set S. Then (17) and (42) reduce to the equations

$$\sum_{l=1}^{n'} w_l\bar{K}(\underline{\kappa}_j,\underline{\kappa}_l)\cdot\bar{C}_1(\underline{\kappa}_l)=\bar{J}_i U_{V_1}(\underline{\kappa}_j,\underline{k}_i)\quad j$$

$$=1,2,\dots,n'\qquad(44)$$

and

$$\bar{f}(\underline{k}_s,\underline{k}_i)=k_0^2\bar{J}_s\cdot\sum_{l=1}^{n'} w_l\bar{C}_1(\underline{\kappa}_l)U_{V_1}(\underline{k}_s,\underline{\kappa}_l).\qquad(45)$$

The matrix equation (44) is solved by applying the lower-upper matrix (LU) decomposition algorithm. Then the values of $\bar{C}_1(\underline{\kappa}_l)$ are substituted into (45) and the scattering amplitude is obtained.

3 COMPUTATION AND CONVERGENCE

3.1 COMPUTATION

Irradiation of a spheroidal RBC by a plane wave of $\lambda=0.6328\ \mu$m (He:Ne laser beam in vacuum) was considered in all runs. We chose a spheroidal instead of a triaxial ellipsoidal (with three different

semiaxes) RBC for ease of prospective comparison with theoretical treatments pertaining to axisymmetric scatterers. This selection does not necessarily affect the computational demands of the program. The index of refraction of the suspending medium was taken as $n_p=1.33$, whereas the complex index of refraction of an RBC relative to the suspending medium was taken as $n_0=\sqrt{\epsilon}=1.04+i\ 10^{-4}$.[18] The mean RBC volume was taken as 90 μm^3.[6] Therefore the mean value of the equivolumetric radius of an RBC was $a\approx2.780\ \mu$m and the size parameter $k_0a\approx36.7$.

In order to implement the previous theoretical analysis, serial and parallel Fortran 77 codes were developed and run on the following shared-memory parallel systems: Silicon Graphics International Inc. (SGI) Power Series 4D/480S (8 × R3000 processors, 70 Mflops), SGI Challenge XL (16 × R4400 processors, 320 Mflops) and SGI Power Challenge XL (14 × R8000 processors, 4200 Mflops). Double-precision arithmetic was used throughout the computation. It was observed that approximately 99% of the total computing time was spent on the calculation of the final matrix elements. Furthermore, the calculation of every matrix element could be performed independently of the calculation of any other matrix element. Thus, resorting to parallel processing for the final matrix elements led to a dramatic decrease in the computing time needed. The speedup depended on both the number of processors used and the overall load of the system during the calculation.

It is pointed out that scattering in the forward direction and in the near-forward angular region is of particular importance to many applications (e.g., ektacytometry, flow cytometry, quantification of sedimentation kinetics). It has also been experimentally proved that light scattered by RBCs is sharply forward peaked.[19] Therefore, we restricted our calculations to the forward and near-forward angular region (up to ±25 deg about the direction of incidence), reducing in this way the computing cost of the analysis. Typical elapsed times for reliable results in this region ranged between 15 min and 6 h in the SG Power Challenge XL system, when six processors were used and the overall load of the machine was medium.

3.2 CONVERGENCE

In order to obtain the scattering diagram [the relative scattered intensity $I=|f(\varphi_{k_s}=\text{const.},\vartheta_{k_s},\varphi_{k_i},\vartheta_{k_i},\varphi_{e_i},\vartheta_{e_i})|^2$ versus the scattering angle ϑ_{k_s}]
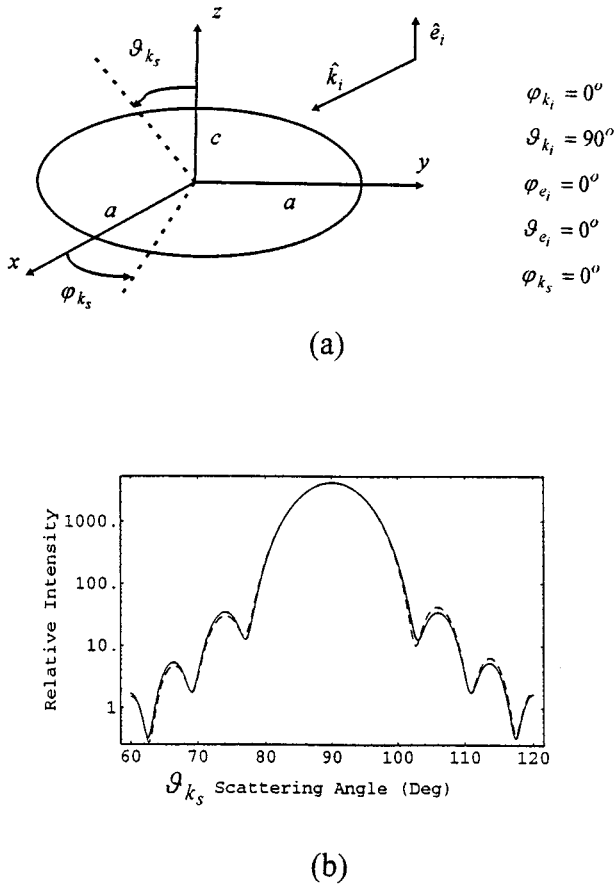
(a)

(b)

Fig. 2 (a) Irradiation geometry of an oblate spheroidal erythrocyte with semiaxes ratio $c/a = 0.335$ and volume $V = 90 \ \mu m^3$. (b) Convergence test. Solid line, case A (six pivot vectors were used); dashed line, case B (seven pivot vectors were used along with larger values for the rest of the discretization parameters).

in the near-forward angular interval, the following numerical approximations were employed. For the calculation of the matrix elements $\bar{\underline{K}}(\underline{k}_1, \underline{k}_2)$, the infinite summations in (20) were truncated at a value $n = m = n\max$. The number of pivot vectors, the number of terms n max in the summations, and the number of integration subintervals in the dx_p and $d\varphi_p$ integrations of (20) were increased until convergence was obtained. Furthermore, the position of pivot vectors was changed until convergence was achieved with the lowest possible computing cost. It was found that pivot vectors forming angles greater than 5 deg with the direction of incidence were of very little significance to the near-forward scattering diagram. Besides, increasing their number led to a sharp increase in the computing time demands of the model. Hence, care was taken to restrict the number of pivot vectors to the smallest possible value without losing significant accuracy in the region of interest. The values of the above-mentioned discretization parameters generally varied from case to case. We give only an indicative list of their values for the case shown in Figure 2. For

curve A (solid line) six pivot vectors were used: one in the forward direction, four equally spaced around the direction of incidence, forming an angle of 0.5 deg with it, and one in the backward direction. $\int_0^1 dx_p$ integration: 10 equal subintervals were used. A 16-point Gauss integration was performed on each one of them. $\int_0^{2\pi} d\varphi_p$ integration: 20 equal subintervals were used as above. For both integrations, a variable step-length routine,[20] which uses a Clenshaw–Curtis quadrature and has a built-in estimate of the absolute error obtained by comparing Newton-Cotes and Romberg estimates, was alternatively used. $n\max = 60$. For curve B (dashed line), seven pivot vectors were used: one in the forward direction, five equally spaced around the direction of incidence, forming an angle of 0.5 deg with it, and one in the backward direction. $\int_0^1 dx_p$ integration: 15 equal subintervals were used. $\int_0^{2\pi} d\varphi_p$ integration: 20 equal subintervals were used. As an alternative, the Clenshaw–Curtis quadrature routine was again used. $n\max = 90$.

3.3 COMPARISON WITH MIE THEORY

A test of the computer program was performed by considering the case of plane electromagnetic wave scattering from a single spherical RBC. The scattering amplitude was calculated by applying both the exact Mie theory[9] and FIEM. The scattering diagrams for values of ϑ_{k_s} between 0 and 180 deg are given in Ref. 21. Six pivot vectors were used in FIEM (one in the forward direction or direction of incidence, four equally spaced around the forward direction and forming an angle of 0.5 deg with it, and one in the backward direction). It has been observed that FIEM compares favorably with Mie theory in the angular interval of up to ± 25 deg around the direction of incidence.

3.4 EKTACYTOMETRY

A further check of the program was provided by producing the diffraction pattern of an oriented monodisperse system of prolate spheroids [Figure 3(b)]. Under certain conditions, such a sytem adequately models erythrocytes suspended in shear flow inside a laser ektacytometer, when used to determine red blood cell deformability. The scattering amplitude $\underline{f}(\underline{k}_s, \underline{k}_i)$ for a prolate spheroid and for a finite number of scattering angles is calculated using the previously described method. The scattering amplitude is calculated for the angular region $\varphi_{k_s} \in [350 \text{ deg}, 360 \text{ deg}] \cup [0 \text{ deg}, 10 \text{ deg}]$ and $\vartheta_{k_s} \in [80 \text{ deg}, 100 \text{ deg}]$. The corresponding solid angle is discretized in such a way that the values of both φ_{k_s} and ϑ_{k_s} are multiples of 1 deg [see Figure 3(a) for the definition of ϑ_{k_s} and φ_{k_s}].

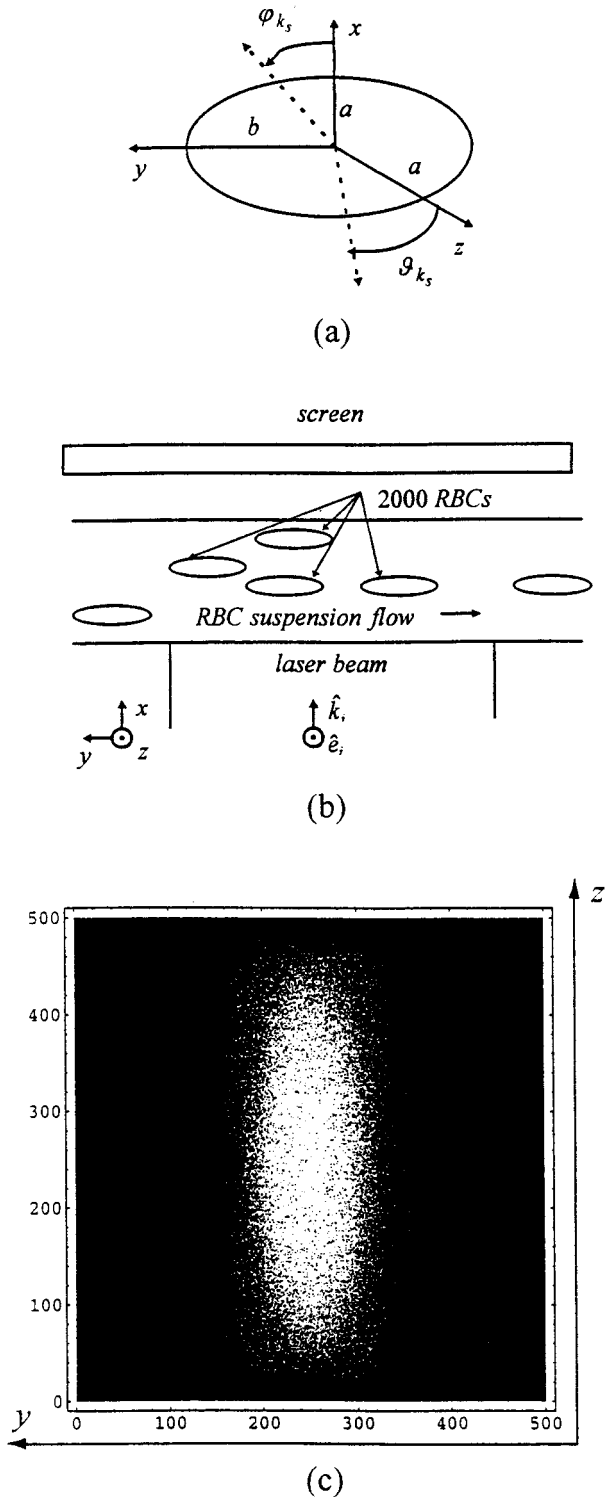A Monte Carlo simulation program for the irradiation geometry of Figure 3(b) was developed in

(a)

$$\varphi_{k_i} = 0''$$
$$\vartheta_{k_i} = 0''$$
$$\varphi_{e_i} = 0''$$
$$\vartheta_{e_i} = 90''$$
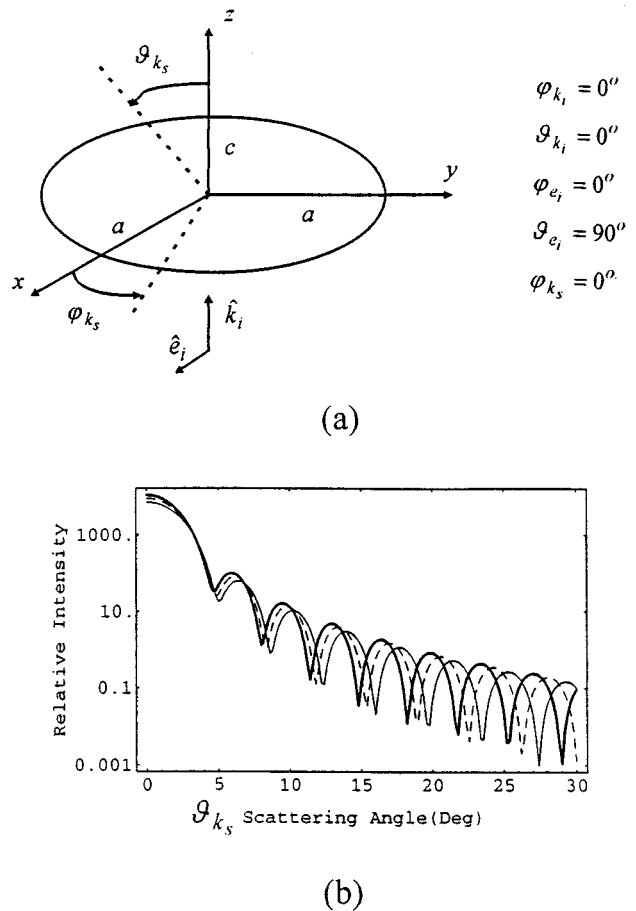$$\varphi_{k_s} = 0''$$

(a)

(b)

(b)

Fig. 4 (a) Irradiation geometry of an oblate spheroidal erythrocyte with semiaxes ratio $c/a = 0.335$. (b) Effect of its volume (V) on the near-forward scattering diagram; thin solid line, $V = 80\ \mu m^3$; dashed line, $V = 90\ \mu m^3$; thick solid line, $V = 100\ \mu m^3$. Six pivot vectors were used.

(c)

Fig. 3 (a) Irradiation geometry of a prolate spheroidal erythrocyte with volume $V = 90\ \mu m^3$ and semiaxes ratio $b/a = 4$. (b) Irradiation geometry of an oriented monodisperse system of prolate spheroidal erythrocytes (Monte Carlo simulation). (c) Diffraction pattern of the system depicted in (b).

which the position of each erythrocyte in the stream was random. A total of 2000 erythrocytes, irradiated by the laser beam at the same time, proved to be sufficient for the reproduction of the expected

diffraction pattern. This number of simultaneously irradiated red blood cells is also typical in actual devices.[22] A more detailed description of the simulation will appear in a separate paper.

In agreement with what has been experimentally observed and theoretically proved by the Van de Hulst anomalous diffraction theory,[8] the diffraction pattern produced by this model [Figure 3(c)] has the following two characteristics. First, the ratio of the major to the minor axis of the first elliptical extinction ring and that of the illuminated cross section of the erythrocyte are equal. Second, the major axis of the diffraction pattern is perpendicular to the streamlines of the shear flow, parallel to which the suspended cells are stretched.

4 NUMERICAL RESULTS

As examples of the potential uses of the model presented, the effects of both the size and the semiaxes ratio of a spheroidal erythrocyte to its scattering diagram are demonstrated. The near-forward scattering diagrams for three different RBC volume values ($V = 80$, 90, and 100 μm^3) and for two different angles of incidence are shown in Figures 4 and 5.
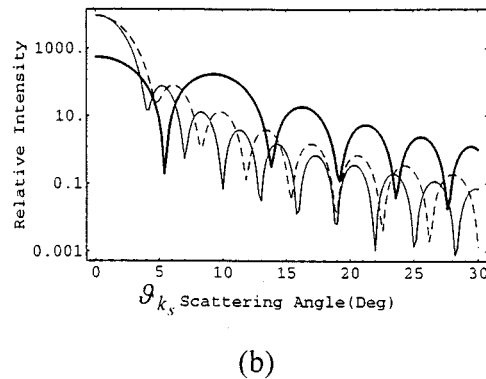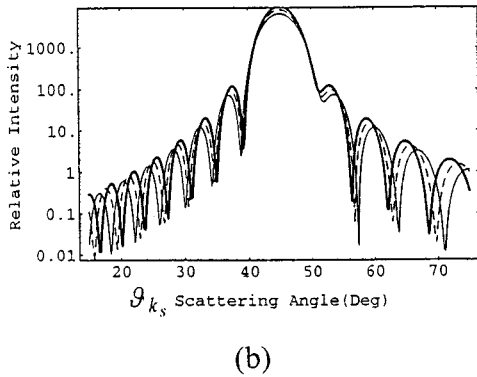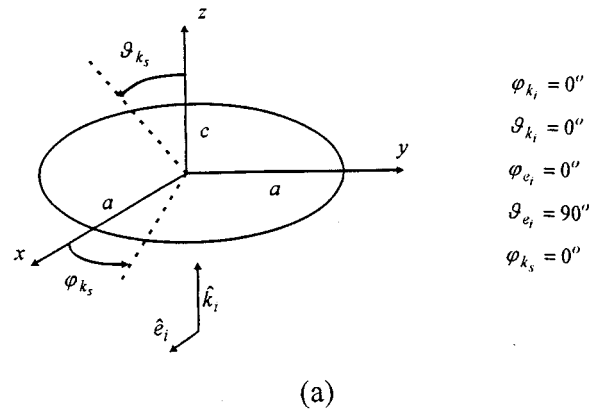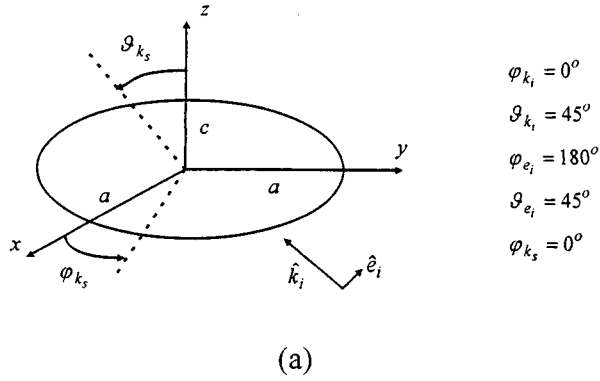
(a)

(b)

Fig. 5 (a) Irradiation geometry of an oblate spheroidal erythrocyte with semiaxes ratio $c/a=0.335$. (b) Effect of its volume (V) on the near-forward scattering diagram; thin solid line, $V=80$ μm^3; dashed line, $V=90$ μm^3; thick solid line, $V=100$ μm^3; six pivot vectors were used.

(a)

(b)

Fig. 6 (a) Irradiation geometry of a spheroidal erythrocyte with volume $V=90$ μm^3. (b) Effect of the semiaxes ratio (c/a) to its near-forward scattering diagram; thin solid line, $c/a=0.2$ (six pivot vectors were used); dashed line, $c/a=0.335$ (six pivot vectors were used); thick solid line, $c/a=4$ (14 pivot vectors were used).

The following characteristics of the scattering diagram for all angles of incidence considered (including the incidence angle of $\vartheta_{k_i}=90$ deg for which the results are not shown in this paper) may be easily noticed. The forward scattered intensity increases with increasing scatterer size, in accordance with Mie theory for large scatterers.[9] The number of lobes in the near-forward scattering diagram also increases with increasing scatterer size.

Furthermore, the near-forward scattering diagrams for three different semiaxes ratios ($c/a=0.2$, 0.335, 4) and for two different angles of incidence are shown in Figures 6 and 7. It appears that the cases considered can be well differentiated (e.g., in flow cytometry) in terms of both the intensity profile of scattered light and the number of lobes in the near-forward scattering diagram.

5 CONCLUSIONS AND FUTURE WORK

A Fredholm integral formalism of light scattering by a triaxial dielectric ellipsoid of complex index of refraction has been developed. Both the position and orientation of the scatterer in a given cartesian coordinate system are considered arbitrary. The analysis has been numerically applied to the case of an ellipsoid with the optical properties of an RBC. It

has been observed that adequate selection of the three semiaxes of the ellipsoid can lead to a satisfactory simulation of certain shapes of abnormal and deformed erythrocytes.

Serial and parallel computer programs have been developed and run on various shared-memory parallel machines. Several tests have ensured the validity of both the analysis and the computer codes. Due to the rather high computational demands of the model, the scattering amplitude only in the near-forward angular region ([−25 deg, +25 deg] around the direction of the incident wave vector) was calculated. Although this region is the most important in ektacytometry and of particular interest in flow cytometry, the scattering amplitude in other scattering angles may be calculated as well. In that case, however, a substantially larger number of pivot vectors would be necessary for those scattering angles and this would result in a very fast increase in computing time. It seems that the use of distributed-memory parallel machines might further improve the efficiency of the model.
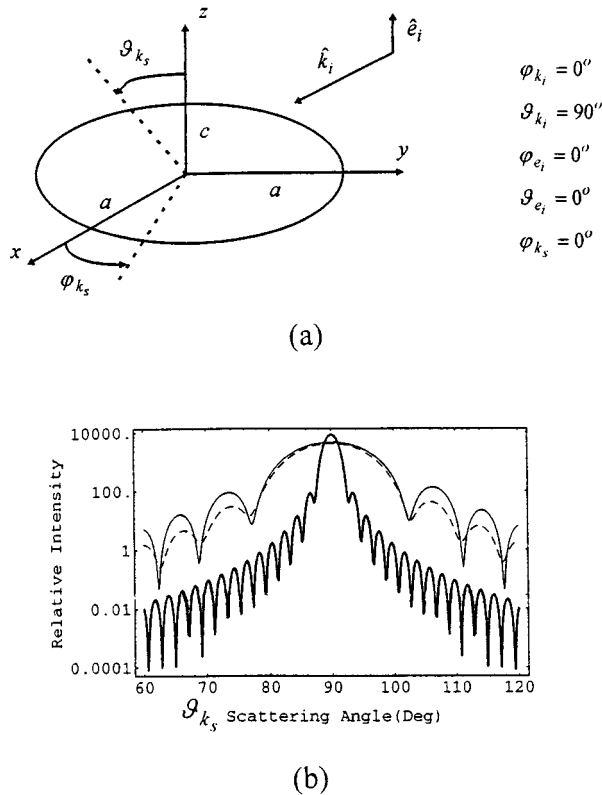
(a)

(b)

Fig. 7 (a) Irradiation geometry of a spheroidal erythrocyte with volume $V = 90 \ \mu m^3$. (b) Effect of the semiaxes ratio (c/a) to the near-forward scattering diagram; thin solid line, $c/a = 0.2$; dashed line, $c/a = 0.335$; thick solid line, $c/a = 4$. Six pivot vectors were used in all cases.

From a practical point of view, the model might be used to generate of a database containing the theoretically predicted scattering diagrams of various forms, orientations, and biochemical composition of a single erythrocyte. The biochemical compositions can be taken into account through the index of refraction. Such a data collection might serve either as the main or as an additional criterion of RBC discrimination in flow cytometers. In Addition, the analysis presented may have some relevance to nonbiomedical fields, such as astrophysics (e.g., light scattering by interstellar dust), atmospheric physics (e.g., light scattering by aerosols), and ocean physics (e.g., light scattering by plankton).

Acknowledgment

REFERENCES

1. H. M. Shapiro, *Practical Flow Cytometry*, Chap.1, Alan R.Liss, New York (1985).
2. M. R. Hardeman, R. M. Bauersachs, and H. J. Meiselman, "RBC laser diffractometry and RBC aggregometry with a rotational viscometer: comparison with rheoscope and Myrene aggregometer," *Clin. Hemorheol.* **8**, 581–593 (1988).
3. G. Wolf, R. Bayer, and D. Ostuni, "Stress-induced rigidification of erythrocytes as determined by laser diffraction and image analysis," *Opt. Eng.* **31**, 1475–1481 (1992).
4. M. R. Hardeman, P. Goedhart, and D. Breederveld, "Laser diffraction ellipsometry of erythrocytes under controlled shear stress using a rotational viscosimeter," *Clin. Chim. Acta.* **165**, 227–234 (1987).
5. M. R. Hardeman, P. T. Goedhart, J. G. Dobbe, and K. P. Lettinga, "Laser-assisted optical rotational cell analyser (L.O.R.C.A); I. A new instrument for measurement of various structural hemorheological parameters," *Clin. Hemorheol.* **14**, 605–618 (1994).
6. W. J. Williams, E. Beutler, A. J. Erslev, and M. A. Lichtman, *Hematology*, pp. 309–316, McGraw-Hill, New York (1990).
7. S. Chien, L. A. Sung, S. Simchon, M. L. L. Lee, K. Jan, and R. Skalak, "Energy balance in red cell interactions," *Ann. New York Acad. Sci.* **416**, 190–206 (1983).
8. G. I. Zahalak and S. P. Sutera, "Fraunhofer diffraction pattern of an oriented monodisperse system of prolate ellipsoids," *J. Colloid Interface Sci.* **82**, 423–429 (1981).
9. M. Born and E. Wolf, *Principles of Optics*, Chap. 13.5, Pergamon Press, Oxford, 1993.
10. B. P. Sinha and R. H. MacPhie, "Electromagnetic scattering by prolate spheroids for plane waves with arbitrary polarization and angle of incidence," *Radio Sci.* **12**, 171–184 (1977).
11. H. C. van de Hulst, *Light Scattering by Small Particles*, pp. 103–113, Dover Publications, New York (1981).
12. N. K. Uzunoglu, *Theoretical calculations of scattering of electromagnetic waves from precipitation particles*, PhD Thesis, University of Essex (1976).
13. A. R. Holt, N. K. Uzunoglu, and B. G. Evans, "An integral equation solution to the scattering of electromagnetic radiation by dielectric spheroids and ellipsoids," *IEEE Trans Antennas Propagat.* **AP-26**, 706–712 (1978).
14. R. G. Newton, *Scattering Theory of Waves and Particles*, Chap. 4(1.2) McGraw Hill, New York (1966).
15. J. J. Tuma, *Dynamics*, Chap. 9, Quantum Publishers, New York (1974).
16. N. Uzunoglu, G. Stamatakos, D. Koutsouris, and D. Yova, "Light scattering by adjacent red blood cells—a mathematical model," *Proc. SPIE* **2326**, 334–345 (1995).
17. G. S. Stamatakos, N. K. Uzunoglu, and D. Yova, "An integral equation solution to the scattering of electromagnetic radiation by a system of two interacting triaxial dielectric ellipsoids. The case of a red blood cell rouleau," *J. Biomedical Opt.* **2**(3), 282–294 (1997).
18. A. Korolevich, A. Ya. Khairullina, and L. P. Shubochkin, "Scattering matrix of a monolayer of optically soft close-packed particles," *Opt. Spectr. (USSR)* **68**(2), 236–239 (1990).
19. A. H. Gandjbakhche, P. Mills, and P. Snabre, "Light-scattering technique for the study of orientation and deformation of red blood cells in a concentrated suspension," *Appl. Opt.* **33**, 1070–1078 (1994).
20. H. O'Hara and F. J. Smith, "The evaluation of definite integrals by interval subdivision," *Comput. J.* **12**, 179–182 (1969).
21. G. S. Stamatakos and N. K. Uzunoglu, "An integral equation solution to the scattering of electromagnetic radiation by a linear chain of interacting dielectric ellipsoids. The case of a red blood cell rouleau," *J. Electromagnetic Waves Appl.* **11**, 949–980 (in press) (1997).
22. K. Murakawa, M. Kohno, Y. Kinoshita, and T. Takeda, "Application of diffractometry and a linear image sensor to measurement of erythrocyte deformability," *Biorheology* **29**, 323–335 (1992).